NANO LETTERS

pubs.acs.org/NanoLett

Letter

Superconducting Vortex-Charge Measurement Using Cavity Electromechanics

Sudhir Kumar Sahu, Supriya Mandal, Sanat Ghosh, Mandar M. Deshmukh, and Vibhor Singh*

Cite This: *Nano Lett.* 2022, 22, 1665−1671

Read Online

ACCESS | Metrics & More | Article Recommendations | Supporting Information

ABSTRACT: As the magnetic field penetrates the surface of a superconductor, it results in the formation of flux vortices. It has been predicted that the flux vortices will have a charged vortex core and create a dipolelike electric field. Such a charge trapping in vortices is particularly enhanced in high-T_c superconductors (HTS). Here, we integrate a mechanical resonator made of a thin flake of HTS $Bi_2Sr_2CaCu_2O_{8+\delta}$ into a microwave circuit to realize a cavity-electromechanical device. Due to the exquisite sensitivity of cavity-based devices to the external forces, we directly detect the charges in the flux vortices by measuring the electromechanical response of the mechanical resonator. Our measurements reveal the strength of surface electric dipole moment due to a single vortex core to be approximately 30 $|e|a_B$, equivalent to a vortex charge per CuO_2 layer of $3.7 \times 10^{-2}|e|$, where a_B is the Bohr radius and e is the electronic charge.

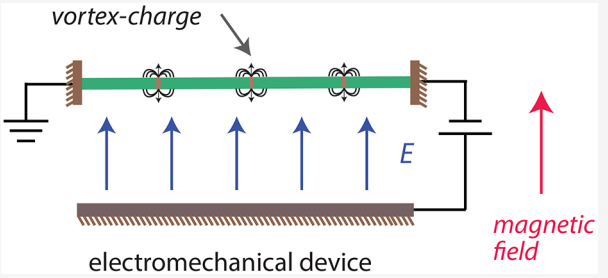

KEYWORDS: *cavity optomechanics, mechanical resonator, high-T_c superconductor, vortex charge, BSCCO*

INTRODUCTION

The penetration of the magnetic field in type-II superconductors in the form of Abrikosov vortices is well-known.[1,2] Such vortices have a normal core of size of the coherence length, and each vortex is surrounded by a circulating supercurrent that decays over a characteristic magnetic length scale. It has been predicted that such vortices can trap charges.[3−6] The origin of the vortex charge can be understood from the difference in the chemical potentials in the superconducting state and the normal region due to the particle−hole asymmetry. It leads to a redistribution of electrons to maintain the same electrochemical potential across a vortex,[7] as shown schematically in Figure 1a. Intuitively, the idea of charged vortex core can also be captured by considering the inertial and Lorentz forces acting on the Cooper pairs encircling the normal core, resulting in the depletion of charges from the core.[6]

To probe the trapped charge in the vortex core, the high-T_c superconductors (HTS) are particularly attractive. The magnitude of the vortex charge is approximately given by $|e|(\Delta/\epsilon_F)^2$, where Δ is the superconducting gap and ϵ_F is the Fermi energy. The ratio Δ/ϵ_F is usually high in HTS ($\Delta/\epsilon_F \sim 0.1$). Indeed, in the past, the inference of the charged vortex core has been made on bulk crystals of cuprate superconductors based on techniques probing the sign reversal of the Hall coefficient,[8] the nuclear quadrupole resonance,[9,10] and instability of the vortex lattice.[11] However, a measurement of the charged vortex core directly measuring its electrostatic field is a challenging task due to its small magnitude and screening by the surrounding charges.

In recent years, nanoelectromechanical systems based approach to probe phase transitions and the thermodynamical properties such as heat capacity, thermal conductivity, and magnetization have drawn a lot of attention.[12−16] Particularly, the integration of exfoliated thin flakes into cavity optomechanical and hybrid devices have resulted into enhanced sensitivity to external forces.[17−19] With these motivations in mind, we apply cavity optomechanical techniques to detect the charges associated with vortices in a high-T_c superconductor by directly probing their electrostatic effect.

RESULTS AND DISCUSSION

In this work, we use a mechanical resonator of 5 unit cell (UC) thick exfoliated flake of $Bi_2Sr_2CaCu_2O_{8+\delta}$ (BSCCO) and integrate it with a microwave cavity to realize a cavity electromechanical device. Due to their low mass, such mechanical resonators have a large coupling with the microwave field of the cavity, which enhances their force sensitivity. Figure 1b shows the electrical equivalent schematic of the device. Such a device is analogous to a Fabry−Perot

Received: December 4, 2021
Revised: February 6, 2022
Published: February 11, 2022

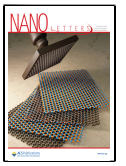

https://doi.org/10.1021/acs.nanolett.1c04688
Nano Lett. 2022, 22, 1665−1671

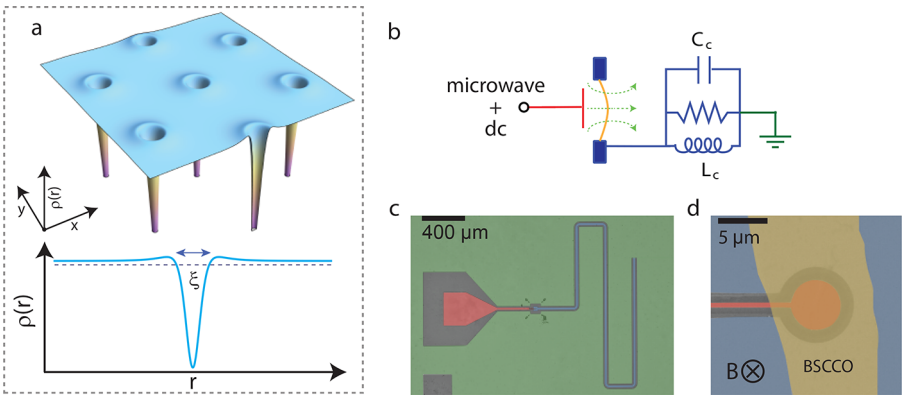

Figure 1. Cavity optomechanical architecture for detecting the vortex charge. (a) Schematic showing the redistribution of the charge density at vortex core due to the chemical potential mismatch in the normal and in the superconducting state. The cyan curve shows the radial profile of the charge density redistribution around the vortex core and indicates the normal core of size of the coherence length ξ. (b) Electromechanical system with a single-port reflection cavity. The device is configured such that both direct current (dc) and microwave signals can be added to the drive port. The equivalent lumped inductance and capacitance are 1.42 nH and 350 fF, respectively. (c) Optical microscope image (false color) of the complete device. It shows a quarter-wavelength reflection-cavity in coplanar waveguide geometry patterned on an intrinsic Si substrate. (d) Scanning electron micrograph (false color) of the device near the coupling capacitor showing the suspended part of BSCCO flake which is 5 UC thick (~15 nm). The circular suspended part has a diameter of 7 μm.

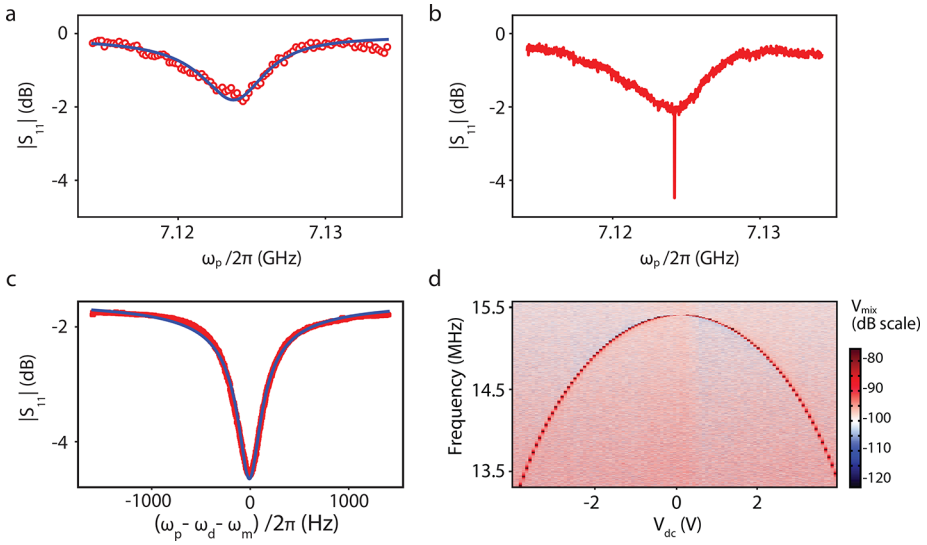

Figure 2. Optomechanically induced absorption (OMIA) measurements: (a) Normalized reflection $|S_{11}(\omega)|$ measurement of cavity at 20 mK. The blue line shows the fitted curve. (b) Measurement of $|S_{11}(\omega)|$ in the presence of a red-detuned pump signal $\omega_d = \omega_c - \omega_m$. The sharp feature at the center of the cavity shows the optomechanically induced absorption (OMIA), resulting from the coherent oscillation of the mechanical resonator. (c) Zoomed-in view of the OMIA feature showing the detailed mechanical response. (d) Color plot of the demodulated signal V_{mix} showing the quadratic tuning of the mechanical resonant frequency with V_{dc} applied at the feedline.

cavity with a mechanically compliant mirror, where vibrations of the mirror parametrically modulate the resonant frequency of the cavity.[20] We use a superconducting coplanar waveguide-based $\lambda/4$ microwave cavity as shown in Figure 1c. The cavity is fabricated by patterning a 200 nm thick sputtered molybdenum and rhenium (MoRe) alloy film on top of intrinsic silicon wafer.[21,22] The MoRe film has a T_c of 11 K. Near the coupler end of the microwave cavity, a feedline is selectively etched to reduce the MoRe film thickness by 120 nm. The difference in MoRe film thickness provides the clearance to form a suspended mechanical drumhead resonator by the transfer of an exfoliated BSCCO flake. A scanning electron microscopy (SEM) image of the suspended BSCCO flake after the transfer is shown in Figure 1d. In this configuration, the BSCCO drumhead-shaped mechanical resonator provides capacitive coupling between the feedline and microwave cavity. In addition, the device design allows application of both alternating current (ac) and direct current (dc) signals through the feedline.

The device is cooled down to 20 mK in a dilution refrigerator with sufficiently attenuated microwave input lines. Additional details of the low-temperature setup are included in the Supporting Information. The reflection from the cavity $|S_{11}(\omega)|$ is measured using a vector network analyzer. Figure 2a shows the measurement of $|S_{11}(\omega)|$ with fundamental resonant mode at $\omega_c/2\pi$ = 7.124 GHz. The solid line is the fit to the cavity response, yielding the internal and external linewidths of $\kappa_i/2\pi$ = 0.48 MHz and $\kappa_e/2\pi$ = 4.92 MHz, respectively.

For mechanical mode characterization, we drive the BSCCO resonator at its fundamental resonant frequency ω_m using the radiation-pressure force. To achieve this, we add a pump signal at $\omega_d = \omega_c - \omega_m$ along with a weak probe signal, ω_p, near ω_c.

https://doi.org/10.1021/acs.nanolett.1c04688
Nano Lett. 2022, 22, 1665−1671

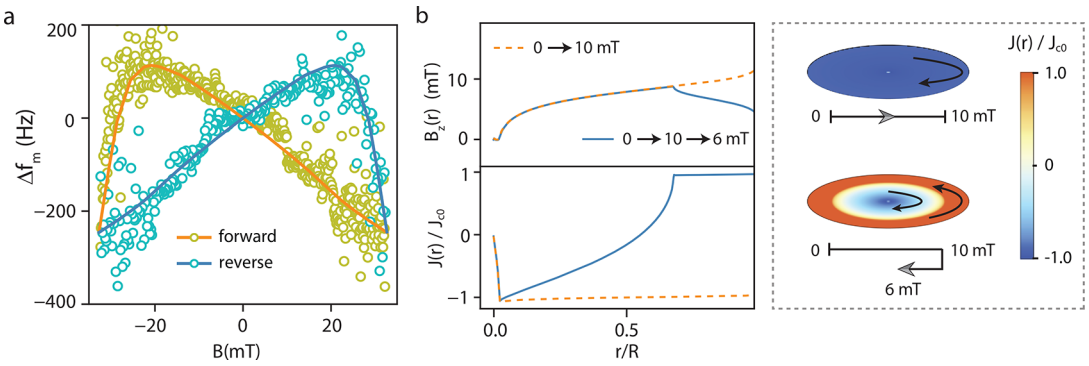

Figure 3. Modification of the mechanical response in the magnetic field: (a) Shift in the mechanical frequency with magnetic field at V_{dc} = 0 V as magnetic field is swept in forward and reverse direction. The solid lines show the results obtained from the critical state model. (b) Plot of calculated local magnetic field and normalized critical current computed in the BSCCO plane. Dotted lines show the spatial profile after a forward sweep of B = 0−10 mT. Solid lines show the profiles for a subsequent field descent to B = 6 mT. The side panel shows a side view of the normalized current distribution for the two cases stressing upon the change in the direction of current as field is lowered after reaching a maximum value.

In the presence of the pump and the probe signals, the mechanical resonator experiences a beating radiation-pressure force near its resonant frequency which drives it coherently.[17,23,24] The mechanical motion of the resonator, in turn, modulates the intracavity pump field, resulting in an upconverted signal exactly at the probe frequency. As a coherent process, the upconverted signal interferes with the original probe signal and therefore results in an interference feature with linewidth set by the mechanical losses. Such interference in the cavity reflection is referred to as optomechanically induced absorption (OMIA).[17,24]

The OMIA interference appears as a sharp absorption feature in the cavity response as shown in Figure 2b. A narrow span measurement of the absorption feature is shown in Figure 2b. The absorption dip directly manifests the coherently driven mechanical response and thus allows the complete characterization of the mechanical resonator. From this measurement, we determine the fundamental mechanical mode frequency of $\omega_m/2\pi \sim 15.383$ MHz and the linewidth of $\gamma_m/2\pi \sim 165$ Hz, corresponding to a quality factor of $Q_m \sim 93\,000$. The high quality factor is a direct indication of the low contact resistance between the MoRe film and BSCCO.[22] For the cavity electromechanical device studied here, we estimated the single photon coupling rate $g_0 = (\partial\omega_c/\partial x)x_{zp}$ to be $2\pi \times 30$ Hz, where x_{zp} is the quantum zero-point motion of the BSCCO resonator.

Due to the novel electrical design of the device, we can add a dc voltage V_{dc} across the capacitor formed by the BSCCO resonator and the MoRe feedline underneath. While such a scheme has a significant advantage for probing the vortex charge,[7] it allows characterization of the BSCCO resonator by an independent technique. A dc signal, V_{dc}, and an ac signal, V_{ac}, can be used to actuate the resonator by a force $C_g V_{dc} V_{ac}/z_0$, where z_0 is the separation between BSCCO and the bottom electrode. By using the cavity as an interferometer, the mechanical mode is detected by demodulating the reflected microwave signal from the cavity. Figure 2d shows the plot of demodulated signal (V_{mix}) as V_{dc} is varied. We observe a quadratic tuning of the mechanical resonant frequency due to capacitive spring softening.[25]

Having described the experimental technique, we measure the electromechanical response when a small magnetic field, perpendicular to the CuO_2 plane of the BSCCO crystal is applied. It is represented in Figure 1d. We perform OMIA measurements while sweeping the magnetic field in the forward and reverse directions. In the presence of the magnetic field, both the cavity frequency and the mechanical resonant frequency can change. Therefore, we first record the cavity response and readjust the pump frequency based on the measurement of $\omega_c(B)$. Figure 3a shows the plot of the mechanical resonant frequency shift $\Delta f_m(B) = f_m(B) - f_m(0)$ at V_{dc} = 0 V. We limit the measurements in the range of ±32.6 mT due to the reduction in the cavity quality factor at higher fields, which obscure the OMIA feature.

The hysteresis in $\Delta f_m(B)$ suggests the role of flux-pinning, the Lorentz force of vortex transferring to the lattice and hence the irreversibility of the frequency shift, similar to the magnetostriction measurements on bulk single crystal of BSCCO.[26] For quantitative analysis, we use the critical state model, which is widely used to explain the magnetization of HTS.[27,28] Here the maximum sheet current is capped at a critical current which in general could be magnetic-field-dependent.[29,30] Due to this sheet current and the local magnetic field $B_z(r)$, the flake experiences a Lorentz force in the lateral direction. It results in a magnetic-field -dependent tension in the flake and hence a change in the mechanical resonant frequency as observed in Figure 3a.

We use a local critical sheet current as $J_c(r) = J_{c0}\exp(-|B_z(r)|/B_0)$, where $B_z(r)$ is the local magnetic field in the BSCCO plane, and the maximum critical current J_{c0} and characteristic magnetic field B_0 are two model parameters.[29,30] We note that here BSCCO resonator thickness (5 UC) is much smaller than the London penetration length.[31] Therefore, a small field can push the flux front, the boundary between the Meissner phase and the mixed phase, to nearly the center of the BSCCO flake. We assume that the steady-state critical currents remain confined to the boundaries of the BSCCO flake. To keep the calculations simple, we treat BSCCO as a thin circular plate. Calculation for the realistic geometry would only result in a scaling factor. Our model neglects geometrical[32] or Bean−Livingston barrier.[33] Furthermore, we assume no interaction between the vortex lines passing through the MoRe film (bottom capacitor plate) and BSCCO resonator (top capacitor plate).

To calculate the force experienced by the suspended part of the BSCCO flake, we first calculate the radial profile of the

https://doi.org/10.1021/acs.nanolett.1c04688
Nano Lett. 2022, 22, 1665−1671

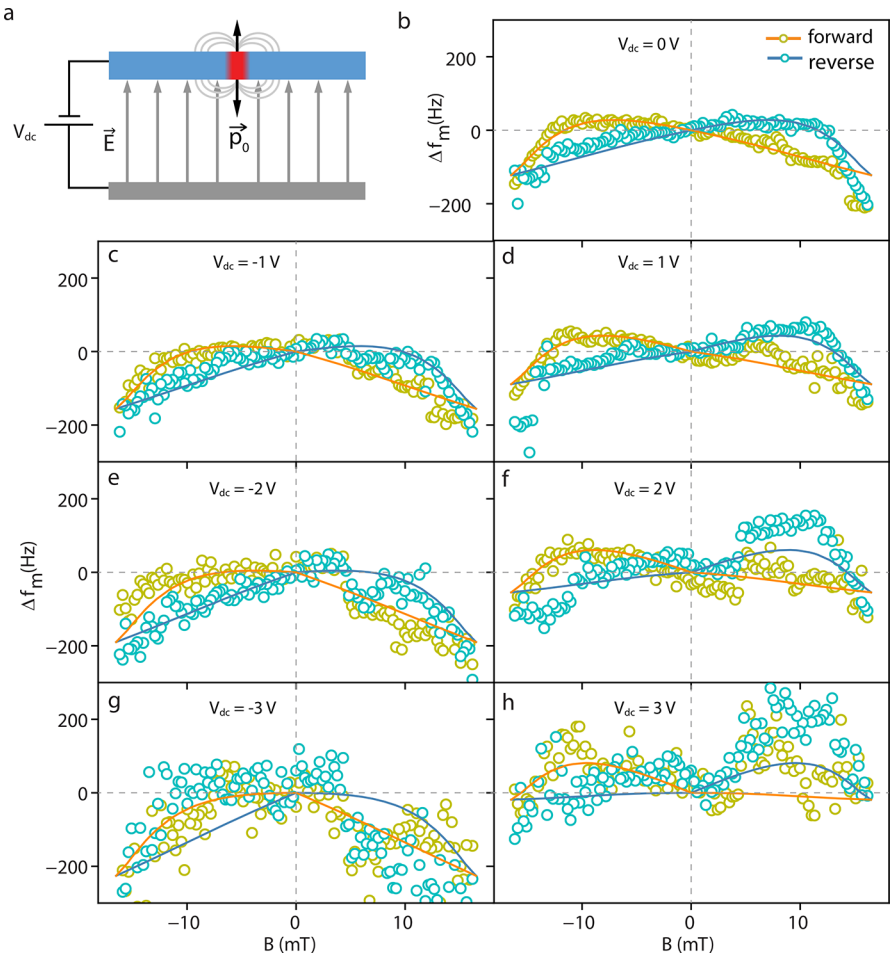

Figure 4. Evidence for the vortex charge. (a) Schematic showing the geometry of the capacitor formed by the BSCCO resonator (cyan) and MoRe plate (gray). The red part of the BSCCO resonator represents a single vortex, showing two surface dipoles. (b–h) Measurement of shift in the mechanical frequency $\Delta f_m = f_m(B, V_{dc}) - f_m(B = 0, V_{dc})$ as the magnetic field is swept in the forward and reverse directions in the presence of a dc voltage, V_{dc}. The solid lines are the calculated curves considering formation of the vortex dipole.

sheet current density, $J(r)$ and $B_z(r)$.[34] The Lorentz force on the suspended part of the BSCCO flake is then estimated by $\int_0^R J(r)\, B_z(r)\, 2\pi r\, dr$, resulting in a net stress in the flake. The stress can be compressive or tensile depending on the sign of the integral. The Lorentz force induced stress can be used to compute the frequency shift of mechanical resonator, as shown by the solid lines in Figure 3a. The radial profiles of the local magnetic field and the normalized critical current are shown in Figure 3b. For these calculations, we have used the critical current density of J_{c0} = 3680 A/μm[35,36] and B_0 = 100 mT.[37] Additional details of the model are included in the Supporting Information.

To probe the charge associated with vortices, their interaction with the electrostatic field setup by a dc voltage plays a crucial role. Therefore, we now turn our focus on the mechanical response when V_{dc} is applied as shown schematically in Figure 4a. The plots of Δf_m at different V_{dc} applied across the BSCCO resonator are shown in Figure 4b–h. For these measurements, we sweep the magnetic field in the ±16.3 mT range due to the reduction in the mechanical quality factor at higher $|V_{dc}|$, which limits the measurement of mechanical response using OMIA technique. The measurement of Δf_m shows a clear asymmetry depending on the sign of V_{dc}. In addition, the overall dispersion with the magnetic field is enhanced at large negative dc voltages as compared to the case when V_{dc} is positive. The asymmetry in the electromechanical response with respect to the sign of V_{dc} (left vs right panels in Figure 4b–h) clearly suggests an electrostatic origin. This could be explained by considering the charge trapped in the vortex core. The charge per copper oxide layer inside the vortex core is given by $Q_c \sim |e|(\Delta/\epsilon_F)^2$.[4,7] Using $\Delta/\epsilon_F \sim 0.1$, and a CuO_2-plane spacing of 0.75 nm for BSCCO,[38] a typical estimate of Q_c = 0.01 $|e|$ can be made. It is equivalent to a line charge density Q_ξ of 0.013 $|e|$/nm.

In the limit $t \gg \xi$, where t is the thickness of BSCCO, the net effect of the vortex line charge can effectively be captured by considering an equivalent surface electric dipole $\vec{p}_0$.[7] To understand our observations, we consider the interaction of surface dipoles $\vec{p}_0$ with the electric field set up by V_{dc}. A dc voltage across the capacitor modifies the interaction energy by $U_{dip}(z) = -\vec{p}_0 \cdot \vec{E}(z)$, where $\vec{E}$ is the electric field between the capacitor plates, and hence leads to an electromechanical coupling. As magnetic field is increased, the number of vortices $n_v(B)$ penetrating the suspended part of the BSCCO increases, as $n_v(B) = (\pi R^2|B|)/\Phi_0$, where Φ_0 is the superconducting flux quantum and R is the radius of the suspended part of BSCCO. By considering a uniform distribution of the vortices on a triangular lattice across the BSCCO resonator, their con-

https://doi.org/10.1021/acs.nanolett.1c04688
Nano Lett. 2022, 22, 1665−1671

tribution to the electromechanical energy can be calculated by summing over all the vortices present in the suspended part.

We include the electric dipole contribution along with the elastic, and the capacitive contribution to the total electromechanical energy $U(z)$. Therefore, the effective spring constant $\partial^2 U(z)/\partial z^2$ and hence the mechanical resonant frequency can be determined. The solid lines in Figure 4b−h show the calculated $\Delta f_m(B)$ by including a dc voltage dependent energy in the electromechanical response. Here the curves are plotted taking a dipole magnitude of $p_0 = 30\ |e|\ a_B$ with a positively charged core, where $a_B = 5.29 \times 10^{-11}$ m is the Bohr radius. It is important to point out here that the sign of the vortex core charge is determined by the oxygen doping level in the BSCCO crystal. For an overdoped (oxygen-rich) crystal, it is expected to be positive.[39] For a positively charged vortex core, the surface dipole moment points in an outward direction from the BSCCO surface regardless to the direction of the applied magnetic field. Therefore, the electromechanical response is expected show an asymmetry with respect to the electric field created by V_{dc}. For a positively charged vortex core, the mechanical resonant frequency is expected to show a softening (hardening) behavior for negative (positive) V_{dc} voltages as observed in the measurement. Details of the electromechanical spring constant calculation are provided in the Supporting Information. In next paragraph, we calculate the line charge density equivalent to this surface dipole moment and make a comparison with the values reported in the literature.

Following ref 7, the charge density profile across a vortex core can be written as $\rho(r) \sim (ea_B\zeta/\pi^3)(\xi^2 - r^2)/(\xi^2 + r^2)^3$, where a_B is the Bohr radius and ζ is the particle−hole asymmetry parameter. The line charge density in the vortex core, therefore, is given by $Q_\xi = \int_0^\xi \rho(r)\, 2\pi r\, dr = \zeta e a_B/(2\pi\xi)^2$. Such a charge redistribution is equivalent to a surface dipole pointing normal to the superconducting surface and having a magnitude of $p_0 = (\zeta e a_B/\pi^2)(m/m_{eff})\ \ln(z/\xi)$. Therefore, the line charge can be related to the dipole moment as $Q_\xi = p_0(m_{eff}/m)(4\xi^2\ \ln(z/\xi))^{-1}$, where m_{eff}/m is the effective mass ratio of the charge carrier. Using $\xi = 3.2$ nm,[40] $m_{eff}/m = 4.6$,[41] and $z = 120$ nm, we obtain $Q_\xi = +4.9 \times 10^{-2}\ |e|$/nm, which is equivalent to a charge of $+3.7 \times 10^{-2}\ |e|$ per CuO_2 layer.

CONCLUSIONS

Our estimation of the charge per copper oxide layer is consistent with the earlier measurements made on YBCO using the nuclear quadrupole resonance technique.[9] Both the experiments reveal a larger value of the vortex charge than that obtained via the theoretical predictions. The difference between the vortex charge magnitude from the experiments and the theory can have several interesting origins. First, it suggests that the gap anisotropy and Fermi surface curvature might be playing an important role.[42] Second, given the ultralow temperature in this experiment, the quantum effects in the vortex could become relevant. Finally, the nature of the vortex core could be different from the metallic phase.[43,44]

To summarize, we show clear evidence for the trapped charges in the vortex core probed using a cavity optomechanical device. The magnitude of the equivalent dipole is higher than the estimates from the BCS-theory while considering Thomas-Fermi screening. Such a difference opens up new possibilities to revisit the vortex charge problem in atomically thin superconductors. Furthermore, our experiment and novel device approach show the advantages of integrating exfoliated thin flake into the cavity optomechanical devices for sensitive measurement of the thermodynamical properties. With minor modifications in the design, such a technique could further be extended to other systems involving topological charge[45] or bosonic Landau levels.[46] This work thus opens up a new avenue to study quantum phase transitions as external parameters are varied.

ASSOCIATED CONTENT

Supporting Information

The Supporting Information is available free of charge at https://pubs.acs.org/doi/10.1021/acs.nanolett.1c04688.

Further information on the experimental setup, cavity characterization, theoretical modeling, and details of data analysis (PDF)

AUTHOR INFORMATION

Corresponding Author

Vibhor Singh − *Department of Physics, Indian Institute of Science, Bangalore 560012, India;* orcid.org/0000-0002-9051-3867; Email: v.singh@iisc.ac.in

Authors

Sudhir Kumar Sahu − *Department of Physics, Indian Institute of Science, Bangalore 560012, India*

Supriya Mandal − *Department of Condensed Matter Physics and Material Sciences, Tata Institute of Fundamental Research, Mumbai 400005, India*

Sanat Ghosh − *Department of Condensed Matter Physics and Material Sciences, Tata Institute of Fundamental Research, Mumbai 400005, India*

Mandar M. Deshmukh − *Department of Condensed Matter Physics and Material Sciences, Tata Institute of Fundamental Research, Mumbai 400005, India;* orcid.org/0000-0002-1401-1080

Complete contact information is available at: https://pubs.acs.org/10.1021/acs.nanolett.1c04688

Notes

The authors declare no competing financial interest.

ACKNOWLEDGMENTS

The authors thank Eli Zeldov, Subir Sachdev, and Vijay Shenoy for insightful discussions. The authors also thank D. Jangade and A. Thamizhavel for their help during the crystal growth. M.M.D. acknowledges the Department of Atomic Energy of the Government of India under Grant No. 12-R&D-TFR-5.10-0100, DST Nanomission under Grant No. SR/NM/NS-45/2016 and SERB CORE grant CRG/2020/003836. V.S. acknowledges the research support under the Core Research Grant CRG/2018/001132 by DST and ISTC-0395 by STC-ISRO. S.K.S. acknowledges device fabrication facilities at the Department of Physics, and CeNSE, IISc-Bangalore funded by Department of Science and Technology (DST), Government of India.

REFERENCES

(1) Ketterson, J. B.; Song, S. N. *Superconductivity*; Cambridge University Press: Cambridge, 1999.

(2) Abrikosov, A. A. Nobel Lecture: Type-II superconductors and the vortex lattice. *Rev. Mod. Phys.* **2004**, *76*, 975−979.
(3) Caroli, C.; De Gennes, P. G.; Matricon, J. Bound Fermion states on a vortex line in a type II superconductor. *Phys. Lett.* **1964**, *9*, 307−309.
(4) Khomskii, D. I.; Freimuth, A. Charged Vortices in High Temperature Superconductors. *Phys. Rev. Lett.* **1995**, *75*, 1384−1386.
(5) Feigel'man, M.; Geshkenbein, V.; Larkin, A.; Vinokur, V. M. Sign change of the flux-flow Hall effect in HTSC. *JETP Lett.* **1995**, *62*, 834−840.
(6) Koláček, J.; Lipavský, P.; Brandt, E. H. Charge Profile in Vortices. *Phys. Rev. Lett.* **2001**, *86*, 312−315.
(7) Blatter, G.; Feigel'man, M.; Geshkenbein, V.; Larkin, A.; van Otterlo, A. Electrostatics of Vortices in Type-II Superconductors. *Phys. Rev. Lett.* **1996**, *77*, 566−569.
(8) Hagen, S. J.; Lobb, C. J.; Greene, R. L.; Eddy, M. Flux-flow Hall effect in superconducting $Tl_2Ba_2CaCu_2O_8$ films. *Phys. Rev. B* **1991**, *43*, 6246−6248.
(9) Kumagai, K.-i.; Nozaki, K.; Matsuda, Y. Charged vortices in high-temperature superconductors probed by NMR. *Phys. Rev. B* **2001**, *63*, 144502.
(10) Mitrović, V. F.; Sigmund, E. E.; Eschrig, M.; Bachman, H. N.; Halperin, W. P.; Reyes, A. P.; Kuhns, P.; Moulton, W. G. Spatially resolved electronic structure inside and outside the vortex cores of a high-temperature superconductor. *Nature* **2001**, *413*, 501−504.
(11) Mounce, A. M.; Oh, S.; Mukhopadhyay, S.; Halperin, W. P.; Reyes, A. P.; Kuhns, P. L.; Fujita, K.; Ishikado, M.; Uchida, S. Charge-induced vortex lattice instability. *Nat. Phys.* **2011**, *7*, 125−128.
(12) Bolle, C. A.; Aksyuk, V.; Pardo, F.; Gammel, P. L.; Zeldov, E.; Bucher, E.; Boie, R.; Bishop, D. J.; Nelson, D. R. Observation of mesoscopic vortex physics using micromechanical oscillators. *Nature* **1999**, *399*, 43−46.
(13) Schwab, K.; Henriksen, E. A.; Worlock, J. M.; Roukes, M. L. Measurement of the quantum of thermal conductance. *Nature* **2000**, *404*, 974−977.
(14) Chen, C.; Deshpande, V. V.; Koshino, M.; Lee, S.; Gondarenko, A.; MacDonald, A. H.; Kim, P.; Hone, J. Modulation of mechanical resonance by chemical potential oscillation in graphene. *Nat. Phys.* **2016**, *12*, 240−244.
(15) Morell, N.; Tepsic, S.; Reserbat-Plantey, A.; Cepellotti, A.; Manca, M.; Epstein, I.; Isacsson, A.; Marie, X.; Mauri, F.; Bachtold, A. Optomechanical Measurement of Thermal Transport in Two-Dimensional MoSe2 Lattices. *Nano Lett.* **2019**, *19*, 3143−3150.
(16) Šiškins, M.; Lee, M.; Mañas-Valero, S.; Coronado, E.; Blanter, Y. M.; van der Zant, H. S. J.; Steeneken, P. G. Magnetic and electronic phase transitions probed by nanomechanical resonators. *Nat. Commun.* **2020**, *11*, 2698.
(17) Singh, V.; Bosman, S. J.; Schneider, B. H.; Blanter, Y. M.; Castellanos-Gomez, A.; Steele, G. A. Optomechanical coupling between a multilayer graphene mechanical resonator and a superconducting microwave cavity. *Nat. Nanotechnol.* **2014**, *9*, 820−824.
(18) Weber, P.; Güttinger, J.; Tsioutsios, I.; Chang, D. E.; Bachtold, A. Coupling Graphene Mechanical Resonators to Superconducting Microwave Cavities. *Nano Lett.* **2014**, *14*, 2854−2860.
(19) Reserbat-Plantey, A.; Schädler, K. G.; Gaudreau, L.; Navickaite, G.; Güttinger, J.; Chang, D.; Toninelli, C.; Bachtold, A.; Koppens, F. H. L. Electromechanical control of nitrogen-vacancy defect emission using graphene NEMS. *Nat. Commun.* **2016**, *7*, 10218.
(20) Aspelmeyer, M.; Kippenberg, T. J.; Marquardt, F. Cavity optomechanics. *Rev. Mod. Phys.* **2014**, *86*, 1391−1452.
(21) Singh, V.; Schneider, B. H.; Bosman, S. J.; Merkx, E. P. J.; Steele, G. A. Molybdenum-rhenium alloy based high-Q superconducting microwave resonators. *Appl. Phys. Lett.* **2014**, *105*, 222601.
(22) Sahu, S. K.; Vaidya, J.; Schmidt, F.; Jangade, D.; Thamizhavel, A.; Steele, G.; Deshmukh, M. M.; Singh, V. Nanoelectromechanical resonators from high-T_c superconducting crystals of $Bi_2Sr_2Ca_1Cu_2O_{8+\delta}$. *2D Materials* **2019**, *6*, 025027.
(23) Weis, S.; Rivière, R.; Deléglise, S.; Gavartin, E.; Arcizet, O.; Schliesser, A.; Kippenberg, T. J. Optomechanically Induced Transparency. *Science* **2010**, *330*, 1520−1523.
(24) Zhou, X.; Hocke, F.; Schliesser, A.; Marx, A.; Huebl, H.; Gross, R.; Kippenberg, T. J. Slowing, advancing and switching of microwave signals using circuit nanoelectromechanics. *Nat. Phys.* **2013**, *9*, 179−184.
(25) Kozinsky, I.; Postma, H. W. C.; Bargatin, I.; Roukes, M. L. Tuning nonlinearity, dynamic range, and frequency of nanomechanical resonators. *Appl. Phys. Lett.* **2006**, *88*, 253101.
(26) Ikuta, H.; Hirota, N.; Nakayama, Y.; Kishio, K.; Kitazawa, K. Giant magnetostriction in $Bi_2Sr_2CaCu_2O_8$ single crystal in the superconducting state and its mechanism. *Phys. Rev. Lett.* **1993**, *70*, 2166−2169.
(27) Bean, C. P. Magnetization of Hard Superconductors. *Phys. Rev. Lett.* **1962**, *8*, 250−253.
(28) Brandt, E. H. Superconductors of finite thickness in a perpendicular magnetic field: Strips and slabs. *Phys. Rev. B* **1996**, *54*, 4246−4264.
(29) Chen, D.; Goldfarb, R. B. Kim model for magnetization of type-II superconductors. *J. Appl. Phys.* **1989**, *66*, 2489−2500.
(30) Senoussi, S.; Osséna, M.; Collin, G.; Campbell, I. A. Exponential H and T decay of the critical current density in $YBa_2Cu_3O_{7-\delta}$ single crystals. *Phys. Rev. B* **1988**, *37*, 9792−9795.
(31) Harshman, D. R.; Kleiman, R. N.; Inui, M.; Espinosa, G. P.; Mitzi, D. B.; Kapitulnik, A.; Pfiz, T.; Williams, D. L. Magnetic penetration depth and flux dynamics in single-crystal $Bi_2Sr_2CaCu_2O_{8+\delta}$. *Phys. Rev. Lett.* **1991**, *67*, 3152−3155.
(32) Zeldov, E.; Larkin, A. I.; Geshkenbein, V. B.; Konczykowski, M.; Majer, D.; Khaykovich, B.; Vinokur, V. M.; Shtrikman, H. Geometrical Barriers in High-Temperature Superconductors. *Phys. Rev. Lett.* **1994**, *73*, 1428−1431.
(33) Bean, C. P.; Livingston, J. D. Surface Barrier in Type-II Superconductors. *Phys. Rev. Lett.* **1964**, *12*, 14−16.
(34) Shantsev, D. V.; Galperin, Y. M.; Johansen, T. H. Thin superconducting disk with B-dependent J_c: Flux and current distributions. *Phys. Rev. B* **1999**, *60*, 13112−13118.
(35) You, L. X.; Yurgens, A.; Winkler, D. Superconducting critical current of a single Cu_2O_4 plane in a $Bi_2Sr_2CaCu_2O_{8+x}$ single crystal. *Phys. Rev. B* **2005**, *71*, 224501.
(36) Stangl, A.; Palau, A.; Deutscher, G.; Obradors, X.; Puig, T. Ultra-high critical current densities of superconducting $YBa_2Cu_3O_{7-\delta}$ thin films in the overdoped state. *Sci. Rep.* **2021**, *11*, 8176.
(37) Sunwong, P.; Higgins, J. S.; Hampshire, D. P. Angular, Temperature, and Strain Dependencies of the Critical Current of DI-BSCCO Tapes in High Magnetic Fields. *IEEE Transactions on Applied Superconductivity* **2011**, *21*, 2840−2844.
(38) Zhao, S. F.; Poccia, N.; Panetta, M. G.; Yu, C.; Johnson, J. W.; Yoo, H.; Zhong, R.; Gu, G.; Watanabe, K.; Taniguchi, T.; Postolova, S. V.; Vinokur, V. M.; Kim, P. Sign-Reversing Hall Effect in Atomically Thin High-Temperature $Bi_{2.1}Sr_{1.9}CaCu_{2.0}O_{8+\delta}$ Superconductors. *Phys. Rev. Lett.* **2019**, *122*, 247001.
(39) Chen, Y.; Wang, Z. D.; Zhu, J.-X.; Ting, C. S. Vortex Charges in High-Temperature Superconductors. *Phys. Rev. Lett.* **2002**, *89*, 217001.
(40) Naughton, M. J.; Yu, R. C.; Davies, P. K.; Fischer, J. E.; Chamberlin, R. V.; Wang, Z. Z.; Jing, T. W.; Ong, N. P.; Chaikin, P. M. Orientational anisotropy of the upper critical field in single-crystal $YBa_2Cu_3o_7$ and $Bi_{2.1}Sr_{1.9}CaCu_{2.0}O_{8+x}$. *Phys. Rev. B* **1988**, *38*, 9280−9283.
(41) Orlando, M. T. D.; Rouver, A. N.; Rocha, J. R.; Cavichini, A. S. Correlation among the effective mass (m*), λ_{ab} and T_c of superconducting cuprates in a Casimir energy scenario. *Phys. Lett. A* **2018**, *382*, 1486−1491.
(42) Ueki, H.; Kohno, W.; Kita, T. Vortex-Core Charging Due to the Lorentz Force in a d-Wave Superconductor. *J. Phys. Soc. Jpn.* **2016**, *85*, 064702.

https://doi.org/10.1021/acs.nanolett.1c04688
Nano Lett. 2022, 22, 1665−1671

(43) Arovas, D. P.; Berlinsky, A. J.; Kallin, C.; Zhang, S.-C. Superconducting Vortex with Antiferromagnetic Core. *Phys. Rev. Lett.* **1997**, *79*, 2871−2874.
(44) Knapp, D.; Kallin, C.; Ghosal, A.; Mansour, S. Antiferromagnetism and charged vortices in high-T_c superconductors. *Phys. Rev. B* **2005**, *71*, 064504.
(45) Jiang, W.; Zhang, X.; Yu, G.; Zhang, W.; Wang, X.; Benjamin Jungfleisch, M.; Pearson, J. E.; Cheng, X.; Heinonen, O.; Wang, K. L.; Zhou, Y.; Hoffmann, A.; te Velthuis, S. G. E. Direct observation of the skyrmion Hall effect. *Nat. Phys.* **2017**, *13*, 162−169.
(46) Devarakonda, A.; Suzuki, T.; Fang, S.; Zhu, J.; Graf, D.; Kriener, M.; Fu, L.; Kaxiras, E.; Checkelsky, J. G. Signatures of bosonic Landau levels in a finite-momentum superconductor. *Nature* **2021**, *599*, 51−56.

https://doi.org/10.1021/acs.nanolett.1c04688
Nano Lett. 2022, 22, 1665−1671